"This is the pre-peer reviewed version of the following article: "Ussia, M., Urso, M., Kment, S., Fialova, T., Klima, K., Dolezelikova, K., & Pumera, M. (2022). Light-Propelled Nanorobots for Facial Titanium Implants Biofilms Removal. Small, 18(22), 2200708", which has been published in final form at https://doi.org/10.1002/smll.202200708. This article may be used for non-commercial purposes in accordance with Wiley Terms and Conditions for Use of Self-Archived Versions."

Black-TiO_2 light-propelled nanorobots for the treatment of multispecies bacterial biofilm on orthodontic titanium implants

Martina Ussia[1], Mario Urso[1], Stepan Kment[2,3], Tatiana Fialova[4], Karel Klima[5], Kristyna Dolezelikova[4,6], Martin Pumera[1,7,8,9]*

[1] Future Energy and Innovation Laboratory, Central European Institute of Technology, Brno University of Technology, Purkyňova 123, Brno 612 00, Czech Republic.

[2] Regional Centre of Advanced Technologies and Materials, Czech Advanced Technology and Research Institute (CATRIN), Palacký University Olomouc, Šlechtitelů 27, Olomouc 783 71, Czech Republic.

[3] Nanotechnology Centre, Centre of Energy and Environmental Technologies, VŠB - Technical University of Ostrava, 17. listopadu 2172/15, 708 00 Ostrava-Poruba, Czech Republic.

[4] Department of Chemistry and Biochemistry, Mendel University in Brno, Zemedelska 1/1665, Brno, 613 00, Czech Republic.

[5] Department of Stomatology – Maxillofacial Surgery, General Teaching Hospital and 1st Faculty of Medicine, Charles University, Katerinska 32, CZ-12808, Prague, Czech Republic.

[6] Center for Zoonotic Diseases, Central European Institute of Technology (CEITEC), University of Veterinary and Pharmaceutical Sciences, Palackeho 1946/1, Brno 612 42, Czech Republic.

[7] Center for Advanced Functional Nanorobots, Department of Inorganic Chemistry, Faculty of Chemical Technology, University of Chemistry and Technology Prague, Technická 5, Prague 166 28, Czech Republic

[8] Center for Nanorobotics and Machine Intelligence, Department of Chemistry and Biochemistry, Mendel University in Brno, Zemedelska 1, CZ-613 00, Brno, Czech Republic.

[9] Department of Medical Research, China Medical University Hospital, China Medical University, No. 91 Hsueh-Shih Road, Taichung, Taiwan.

E-mail: martin.pumera@ceitec.vutbr.cz

Abstract

Titanium miniplates are biocompatible materials employed in modern orthodontics as indispensable tools for transmucosal anchorage on the buccal cortical bone of the mandible or maxilla. However, plate removal is often required due to implant complications. Among them, biofilm formation in the oral cavity is associated with severe inflammation of boundary tissue which frequently result in the implant failure, especially in those cases of antibiotic resistance. In light of this, new strategies to control or treat oral bacterial biofilm are of high interest. Herein, for the first time we exploited the ability of nanorobots against multispecies bacterial biofilm grown onto orthodontic commercial titanium miniplate implants to simulate pathogenic conditions of the oral microenvironment. The strategy is based on the use of light-driven self-propelled tubular black-TiO_2/Ag (B-TiO_2/Ag) nanorobots, that unlike traditional ones, exhibit an extended absorption and motion actuation from UV to the visible-light range. The motion analysis was performed separately over UV, blue and green lights irradiation and showed different motion behaviors, including a fast rotational motion that decreased with increasing wavelengths. The biomass reduction was monitored by evaluating LIVE/DEAD fluorescent and digital microscope images of bacterial biofilm treated with the nanorobots under motion and no-motion conditions. The current study and the obtained results can bring significant improvements for effective orthodontic therapies.

Introduction

Nowadays, medicine's development has reached a high level of complexity to enhance life span and quality. Patients often need surgery to implant external artificial bodies to achieve this goal, thus involving complicated procedures and prevention actions. In this context, endosseous oral implants became crucial tools in dental and

maxillofacial surgery to restore extra- and intraoral defects, or simply to replace accidentally lost teeth[1–4]. On the other hand, oral bacterial biofilm-related diseases are considered the most severe clinical problem and are one of the primary causes of implants failure[5,6]. After exposure of dental implants to the oral cavity microenvironment, the strong interaction between saliva components, bacterial and host tissue products causes the formation of a pellicle on the implant surface within 30 minutes that acts as an ideal substrate for bacterial colonization. After that, cell-to-cell adhesion of secondary colonizers induces the growth and accumulation of bacterial biofilm around orthodontic implants[7]. Once the biofilm is formed, it is complicated to eradicate. It refers to a complex, functionally, and structurally organized structure in which microorganisms cooperate as a community becoming more resistant to antibodies, phagocytes, and antibiotics. Consequently, bacterial biofilm induces peri-implantisis infections, whose clinical manifestations include inflammation of the adjacent mucosa, bone resorption, and the subsequent implant loss[6,8].

In light of this, most of the efforts are devoted to preventing biofilm formation *via* the development of advanced biomaterials because bacterial colonization is directly associated with implant surface features (hydrophobicity, chemical composition, porosity, and shape)[9]. However, it is worth noting that about 700 bacterial species can form biofilm in the oral cavity, and about 400 species are capable of adhesion on orthodontic implants, making the design of multimodal antimicrobial surfaces significantly challenging, especially in finding a good compromise from a scientific and economic point of view[5,8]. Titanium implants are still the most widely used tools for clinical practice because of their remarkable bioactivity, corrosion resistance, and unique mechanical properties, although biomaterials with poor anti-adherent abilities or contact killing effects[5]. Therefore, novel and alternative antimicrobial strategies are needed to treat mature bacterial biofilm around the implant, reducing at the same time local planktonic (free) bacteria in the oral cavity microenvironment[10].

Recently, as the emerging materials in nanomedicine, nanorobots are triggering increasing interest. They are autonomous machines at the small scale that can be propelled converting several energy sources such as chemical fuels, magnetic field, acoustic field, and light into mechanical energy[11–14]. Self-propelled nanorobots are aimed to succeed where conventional nanomedicine fails. For example, micro- and nanorobots can provide real-time diseases detection[15,16], monitoring[17,] and treatment, or on-demand release of drugs, reactive species and bactericidal agents[18]. They can serve as miniaturized surgery to repair damaged cells and their scaled-

down size allow working operation in remotes areas without losing their physico-chemical characteristics and functionalities. Among them, photocatalytic nanorobots are of particular interest since their motion can be controlled by irradiation or adjusting the incident light[19,20].They also possess the ability to generate and release reactive oxygen species (ROS) capable to initiate photodegradation processes for improved therapeutic outcomes[15,21]. Recently, significant attention has also been devoted towards nanorobots that can be actuated by any portion of the available light spectrum to adapt them to the specific application[22].

Black-TiO_2 (B-TiO_2) is one of the best candidate due to its absorption broad band, from UV range to the near infrared (NIR) region, maintaining at the same time its photocatalytic ability and biocompatibility[23,24]. To the best of our knowledge, there is only one report describing the study of B-TiO_2 as micromotors. A Janus microsphere of Au/B-TiO_2 was tested by a broad range of light absorption wavelengths (300-800 nm), reporting directional motion behaviors with speed in the range of 3 - 30 μm/s for five different light sources, in presence of 3% of H_2O_2[22].

Herein we present a first example of light-driven self-propelled tubular nanorobots based on B-TiO_2 decorated with Ag nanoparticles (NPs) by physical deposition to degrade bacterial biofilm growth on commercial orthodontic titanium miniplate implants (see **Scheme 1**). The motion of the nanorobots was tested under UV-light and the narrow-banded regions of blue (450-500 nm) and green (540-550 nm) lights, showing a multitude of motion modes (rotational, circular, and random) depending on the mutual orientation of B-TiO_2 nanotubes with respect to the metal target during the deposition. Interestingly, the fast rotational and random autonomous motions of B-TiO_2/Ag nanorobots make them ideal candidates as biocompatible devices demonstrating superior antibacterial activity through the enhanced release of ROS and Ag ions under light irradiation. Therefore, multispecies bacterial biofilm composed of typical gram-negative early bacterial colonizers of the oral microenvironment and antibiotic-resistant gram-positive bacteria was directly grown onto commercial orthodontic implants, thus exposed to the nanorobots under motion and no-motion conditions to evaluate their antibiofilm capabilities.

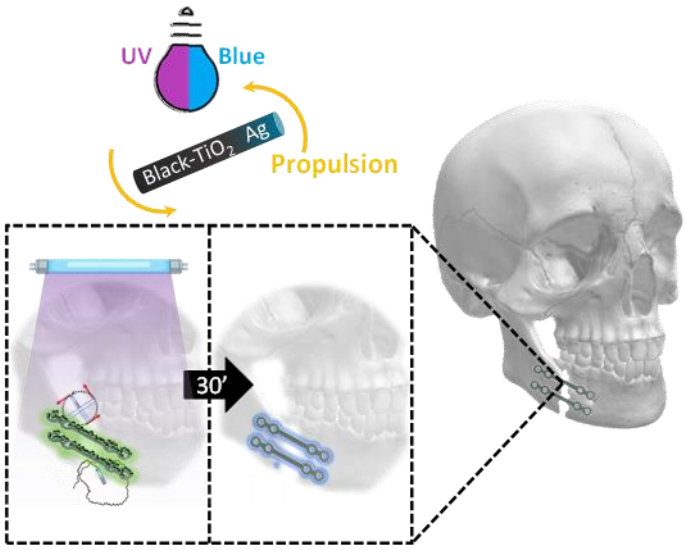

Scheme 1. Light-driven self-propelled tubular B-TiO_2/Ag nanorobots to remove multispecies biofilm from orthodontic titanium miniplates routinely practiced in oral and maxillofacial surgery.

Results & Discussion

Fabrication, characterization, and motion analysis of B-TiO_2/Ag nanorobots

Fabrication of B-TiO_2/Ag nanorobots began by preparing TiO_2 nanotubes through electrochemical anodization of titanium foil. The TiO_2 nanotubes were calcinated at 450°C to induce the most photoactive anatase phase formation[25]. After that, to extend the absorption capabilities in the visible region of the spectra, the TiO_2 nanotubes were converted in the corresponding B-TiO_2 *via* thermal reduction under H_2 atmosphere at 450°C. At this stage, UV-Vis analysis was used to confirm the TiO_2 conversion. As shown in Figure S1 (Supporting Information), clear broadband in the visible range of B-TiO_2 has been measured after the reduction process. Once B-TiO_2 was realized, the nanotubes were decorated with Ag NPs. The resulting B-TiO_2/Ag nanotubes were finally released from the titanium template by manually scratching.

Figure 1 summarizes the different fabrication steps of B-TiO_2/Ag nanorobots, and reports top and cross-view scanning electron microscopy (SEM) images of B-TiO_2/Ag together with EDX mapping for compositional analysis. As it is possible to appreciate, the B-TiO_2/Ag nanotubes possess a diameter of about 400 nm and the cross-view EDX image clearly shows how Ag NPs are able to cover only the upper part of the nanotubes because of their short distance. Interestingly, the B-TiO_2 nanotubes do not present a homogenous growth and result in a compact B-TiO_2 layer close to the titanium sheet to end as thin, separated nanotubes.

During the detachment, because of their fragility, only the upper section is removed from the template composed of the asymmetrical B-TiO_2/Ag structures with a maximum length of about 3 μm.

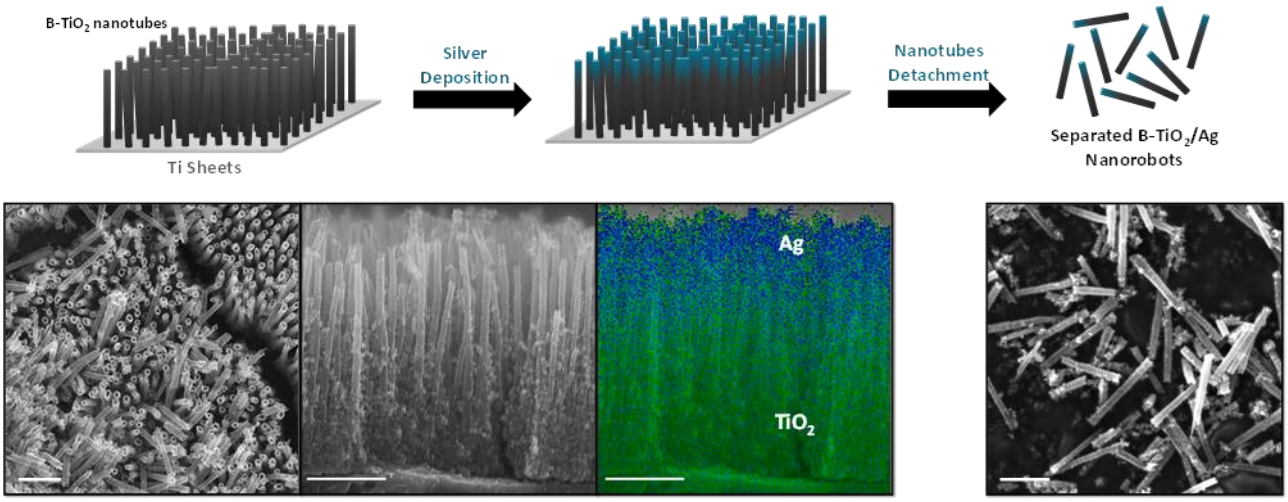

Figure 1. Fabrication and characterization of B-TiO_2/Ag nanorobots. Schematic representation of the B-TiO_2/Ag nanorobots fabrication steps and the corresponding cross-view SEM-EDX image and the top-view and cross-view SEM images before and after the nanorobots detachment from Ti sheets. Scale bars are 2 μm.

As mentioned before, the absorption band of B-TiO_2 occurs over the whole visible wavelength spectrum (400-800 nm), suggesting that the self-propulsion abilities of the B-TiO_2/Ag nanorobots can also be triggered in the visible range. Due to this, the motion of the nanorobots was tested under UV-light and in different regions of the visible spectrum (blue and green light regions).

The motion of the as-prepared B-TiO_2/Ag nanorobots under UV irradiation was optically monitored and recorded through a charge coupled device (CCD) video camera at 50 fps. It showed self-propulsion when irradiated under UV-light and in the presence of a very low concentration of H_2O_2 (0.025, 0.05, and 0.1%). At the same time, B-TiO_2 nanotubes did not experience any autonomous movement under the same experimental conditions in a control experiment. Similar to most of the photocatalytic micromotors reported in the literature so far[11,18,19], the motion mechanism is based on the light-induced decomposition of H_2O_2 at the nanorobots/solution interface. In particular, B-TiO_2 absorbs light with energy equal to or higher than its bandgap to produce photogenerated electron-hole pairs. Electrons in the conduction bands are rapidly transferred to the Ag side, hindering electron-hole recombination phenomena in the semiconductor. Photogenerated holes in B-TiO_2 decompose H_2O_2 in O_2 and protons (H^+). Contemporarily, H_2O_2 and protons

are reduced to water at the Ag side. The resulting protons gradient establishes a local electric field which causes the nanorobots to propel via the self-electrophoretic mechanism.

Interestingly, B-TiO_2/Ag nanorobots showed multiple motion modes under UV irradiation, displaying also stop-go motion by switching on-off the light (see **Movie S1**). These can be categorized in three main behaviors, which are shown in the three rows of time-resolved images in **Figure 2a**, acquired for B-TiO_2/Ag nanorobots irradiated by a 365 nm UV LED (1.6 mW cm^{-2}) in the presence of 0.1% H_2O_2. The top row represents a rotational motion mode in the same position resembling that of clock's hands, in which B-TiO_2/Ag nanorobots rotate around a pin corresponding to one of their ends. The nanoparticles were manually tracked with ImageJ software, calculating a rotational speed of about 500 ±173 rpm min^{-1}. The middle row presents nanorobots that swim along the nanotube axis and change direction randomly, reaching speeds as high as 31 ± 11 µm s^{-1}. The bottom row illustrates the third motion type, the rarest, which can be defined as an intermediate situation between the two previous limit cases. In fact, nanorobots rotate. But differently from the first rotational motion mode, there is no fixed point during their rotation. Instead, they move along the nanotube axis describing circular trajectories. **Figure 2b** represents the displacement of the nanotubes along the x-axis as a function of time which allow to distinguish the differences between the rotational and circular modes.

For the two limit cases, the motion was further characterized at a lower percentage of H_2O_2 to find the minimum amount to initiate nanorobots propulsion. **Figure 2c** shows that a significant displacement is registered at the very low concentration of 0.025% of H_2O_2, making the B-TiO_2/Ag nanorobots promising for biological applications. As expected, the motion speed increases with the fuel concentration because of the higher decomposition rate at the B-TiO_2 side[11]. In particular, the rotating nanotubes move at 240 ± 76 rpm min^{-1} and 390 ± 126 rpm min^{-1}, and the random swimmers at 8 ± 1 and 23 ± 9 µm s^{-1}, using 0.025 and 0.05% H_2O_2, respectively.

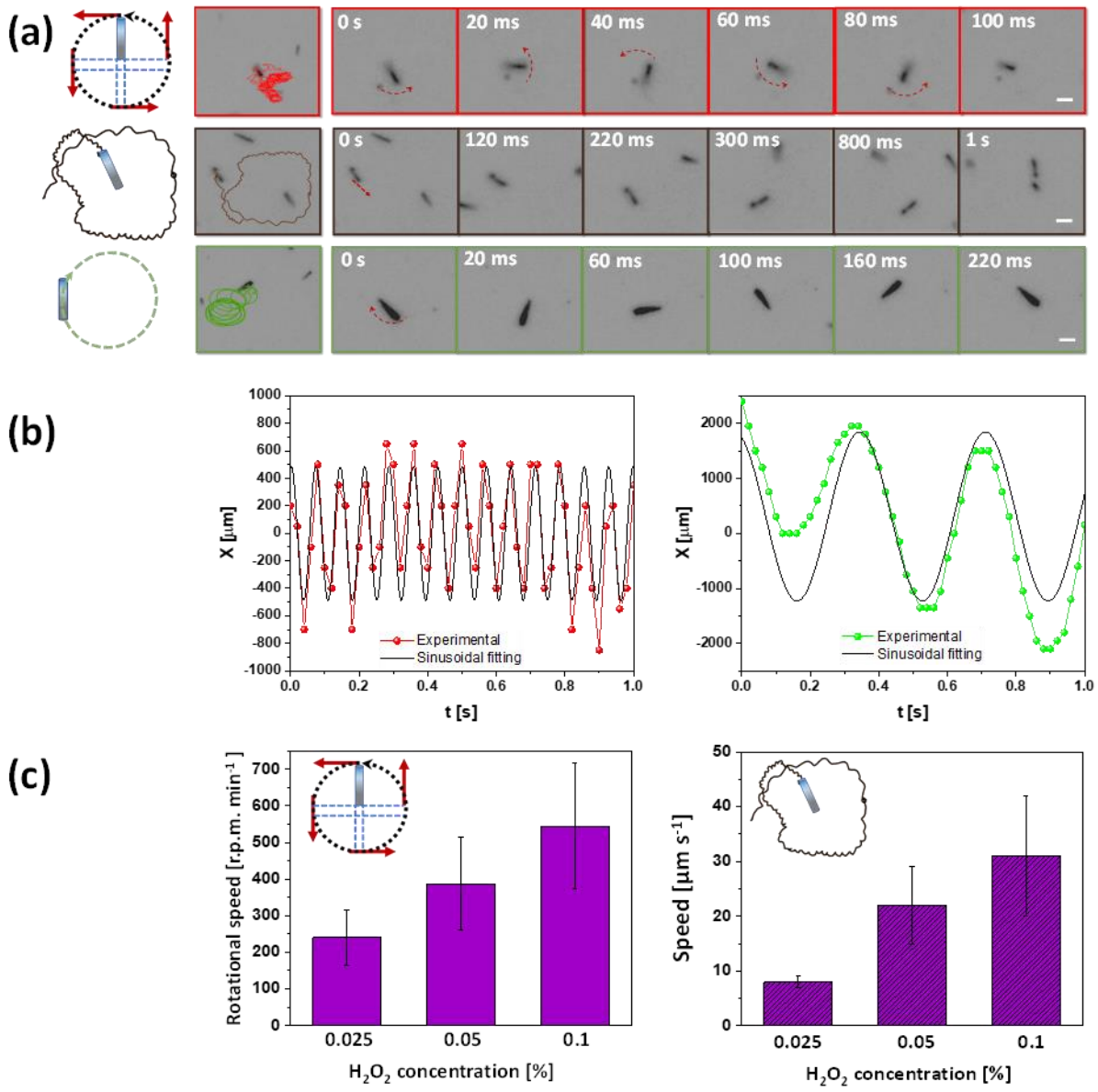

Figure 2. Motion studies of the B-TiO_2/Ag nanorobots. **(a)** Representative trajectories and time-frame images of rotational, random, and circular motion of B-TiO_2/Ag nanorobots after exposure of to UV-light irradiation in 0.1% of H_2O_2. **(b)** Displacement of B-TiO_2/Ag nanorobots as a function of the time for rotational (left panel) and circular (right panel) motion behaviors. **(c)** Speed of B-TiO_2/Ag nanorobots exposed to UV-light irradiation (1.6 mW cm^{-2}) in different concentrations of H_2O_2 for rotational (left panel) and random motion (right panel) behaviors. Scale bars are 5µm.

These multiple motion behaviors are attributed to different configurations of the deposited Ag layer on B-TiO_2 nanotubes. Both plan and cross-view SEM images in **Figure 1** show that B-TiO_2 nanotubes were not aligned along a specific direction with respect to the substrate plane. Indeed, some of them grew perpendicularly to the substrate, while the others were randomly oriented. The Ag layer was deposited by placing the substrate in front of the Ag target. Consequently, the deposition occurred only on nanotubes' surface that was directly exposed to the target. On this basis, it is reasonably assumed that the Ag deposition

was more symmetric on nanotubes perpendicular to the substrate than for those inclined due to a shadowing effect. The higher the inclination of the nanotube, the more pronounced was the asymmetry. Then, nanorobots originated from perpendicular nanotubes moved along the direction of their axis due to the symmetric Ag deposition, while those based on inclined nanotubes showed the rotational motion. Owing to the variety of nanotubes inclinations, many rotational modes were observed, ranging from the rotation around a pin to the circular motion.

The proposed explanation was corroborated by a numerical simulation of the H^+ production at the B-TiO_2 side due to the reaction between H_2O_2 and photogenerated holes in B-TiO_2 under 0.1 s light irradiation. Despite not considering the simultaneous H^+ consumption at the Ag side, this study provides valuable information about the form of the H^+ gradient responsible for nanorobots' movement. The simulation was conducted for the two configurations illustrated in **Figure 3(a)**, corresponding to nanotubes with an asymmetric (left) and symmetric (right) Ag coating reflecting the two limit cases mentioned above. It is noted that the simulation was performed on nanorods rather than nanotubes for simplicity. **Figure 3(b)** displays the simulated H^+ concentration spatial distribution for the two configurations. The asymmetric Ag coating generates a nonuniform H^+ distribution which, in turn, induces the rotation of the nanorobot. In contrast, the symmetry of the Ag coating is reflected in a uniform H^+ distribution around the nanorobot, which swims along its axis.

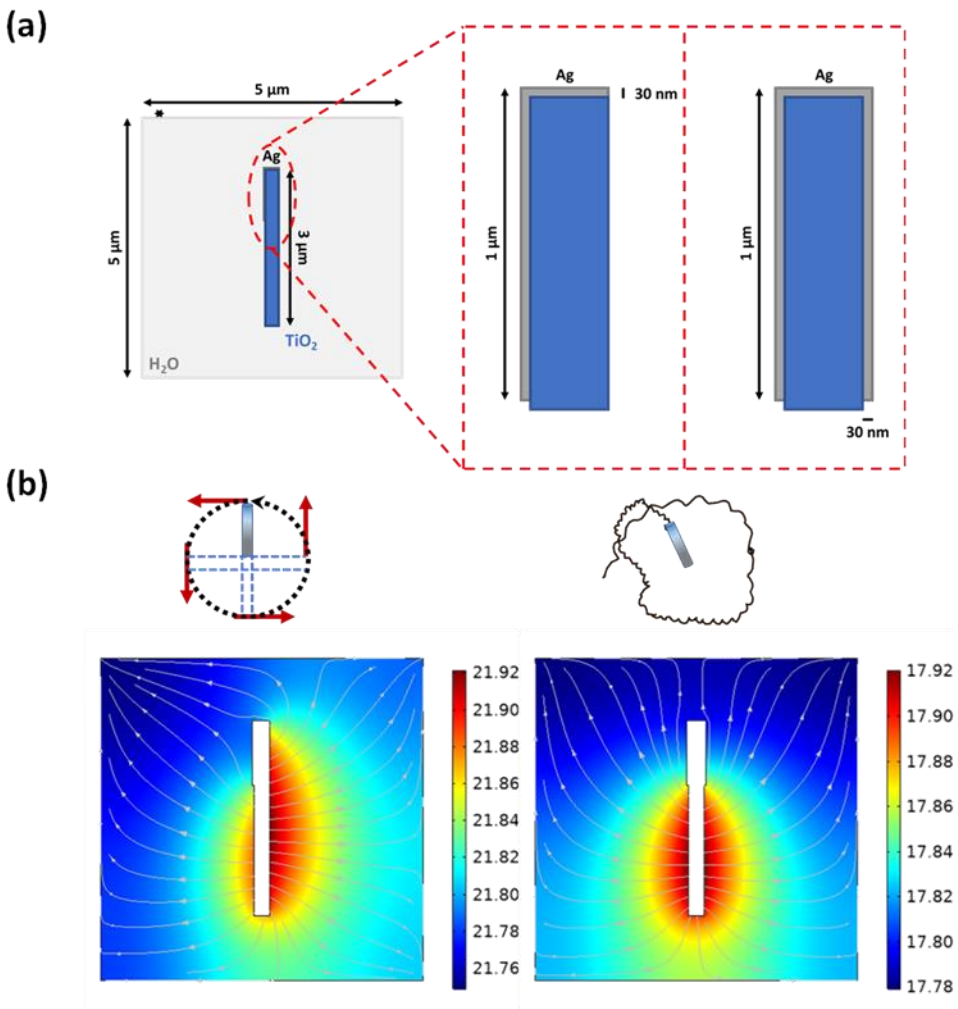

Figure 3. Numerical simulation of the H^+ gradient distribution produced at the B-TiO_2 side due to the reaction between H_2O_2 and photogenerated holes in B-TiO_2 under 0.1s light irradiation. **(a)** Scheme of the two configurations of B-TiO_2 nanotubes with an asymmetric (left panel) and symmetric (right panel) Ag coating. **(b)** Simulated H^+ gradient spatial distribution for the two configurations.

The motion of B-TiO_2/Ag nanorobots in the visible range was studied by their exposure to blue (450-500 nm) and green (520-550 nm) lights, separately through a filter cube. A significant displacement with stop-go motion was observed only under blue light irradiation and in the presence of at least 1% of H_2O_2 (see **Figure 4a**), recording a maximum speed of 11 ± 3 µm s^{-1} at 5% H_2O_2. These results suggested the ability of the nanorobots to be propelled in the visible range. Despite the increased absorption behavior observed in the visible range at a wavelength higher than 500 nm (see **Figure S1**), faster surface recombination phenomena of the photogenerated electro-hole pairs may cause a negligible motor speed in the green-light region (see **Movie S2**).[22]

Figure 4b shows the mean square displacement (MSD) as a function of the time relative to the nanorobots motion under UV light in 0.1% H_2O_2 and under blue light in 2.5 and 5% H_2O_2. It is worth noting that the MSD for UV-propelled nanorobots was calculated by selecting only particles presenting the random motion. The MSD plots fitted with parabolic curves for nanorobots moved under both blue and UV-light. Whereas, the MSD plot for UV propelled B-TiO_2/Ag displayed a decrease in R-square, mainly due to the rotational motion's contribution (see **Figure 4d**) overlapped to the random motion, as previously discussed. **Movie S3** and **Figure 4c** show how the blue-light propelled nanorobots did not show the peculiar multimodal motion mode observed in the case of UV-light activation, especially with H_2O_2 percentage lower than 5%.

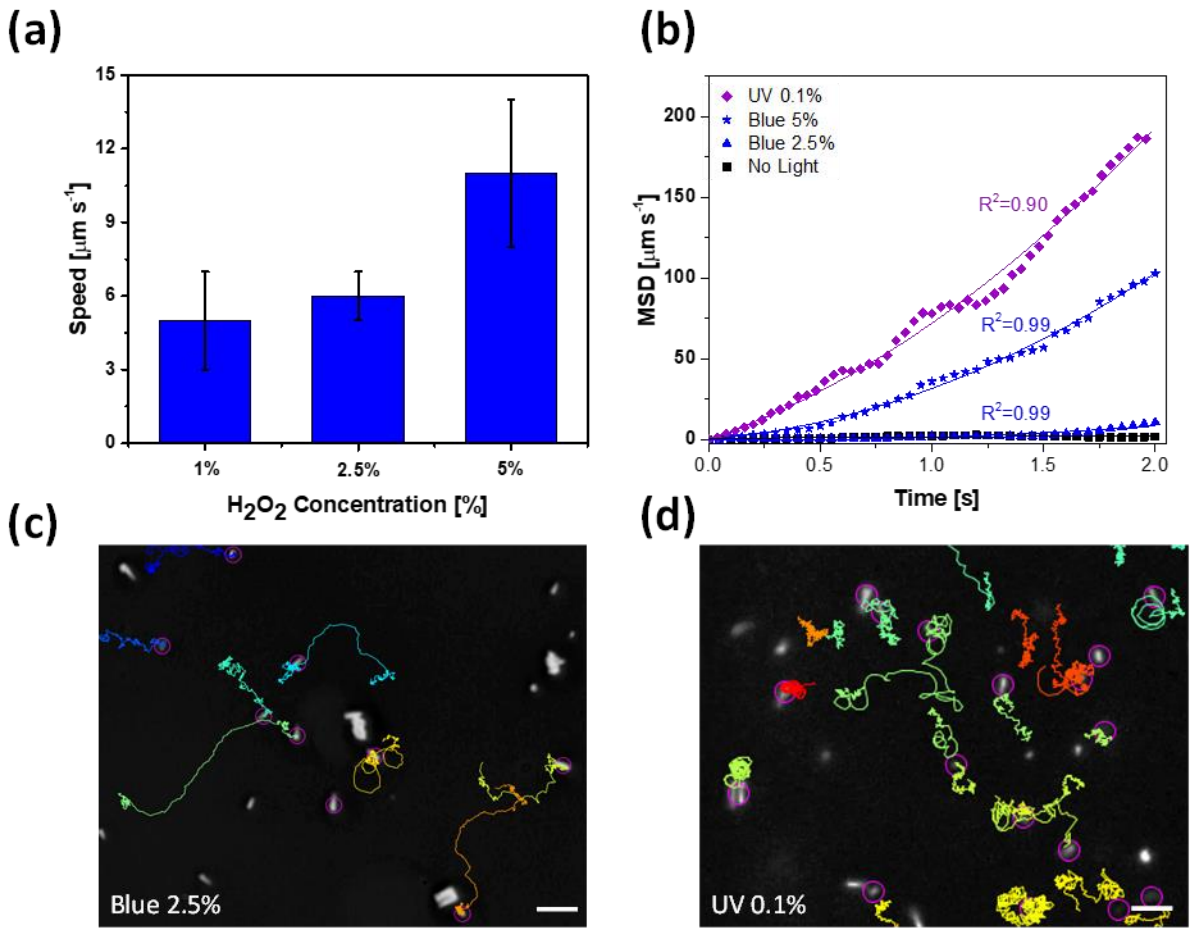

Figure 4. Motion analysis of B-TiO_2/Ag nanorobots under blue light (420-450 nm) irradiation. **(a)** Speed of the nanorobots at different H_2O_2 concentrations. **(b)** Plot of the mean square displacement versus time of nanorobots propelled under UV- and blue-light irradiation with different H_2O_2 concentrations. Snapshot of B-TiO_2/Ag nanorobots tracking showing their trajectories for 5 s under **(c)** blue-light irradiation in 2.5% of H_2O_2 and **(d)** UV-light irradiation in 0.1% H_2O_2. Scale bars are 10 μm.

Performances of B-TiO_2/Ag nanorobots to reduce multispecies biofilm on titanium miniplate implants

The unique human oral microenvironment allows the adhesion of bacteria on natural teeth and any host biomaterial placed in the mouth. Upon completion of soft tissue integration of endosseous implants, dysbiosis of the microflora that populates the oral cavity favors the formation of bacterial biofilm, the preferred method of bacteria growth. It is well known that microorganisms in the biofilm can easily exchange nutrients and protect them from competing microbes[1,5]. Importantly, dental plaque comprises more than 500 species of bacteria. Around the dental implant, the microbial diversity rapidly increases through a coaggregation mechanism between early and secondary bacteria colonizers, resulting in a multispecies biofilm that is more difficult to eradicate, especially when bacteria establish antibiotic resistance[26].

In light of this, the bactericidal effect of B-TiO_2/Ag nanorobots was tested against a biofilm composed of three bacterial species. Two of these have been identified as typical early colonizers in orthodontic implants: the facultative anaerobes *Aggregatibacter actinomycetemcomitans* (gram-negative) and *Streptococcus mutans* (gram-positive)[26]. The third specie used in this work is the gram-positive Methicillin-resistant *Staphylococcus aureus* (MRSA), responsible for recidivating infections in humans and difficult to treat due to its antibiotic-resistance.

Figure 5 (on the left) shows preliminary tests of the antibiofilm activity of B-TiO_2/Ag nanorobots. During the experiment we induced the motion by UV-light irradiation due to the lower amount of H_2O_2 to be used and the best motion performance as previously described. In a first step we estimated the minimum inhibitory concentration (MIC) of BTiO_2/Ag nanorobots. For this purpose, bacterial biofilm was grown onto polystyrene 96 well plate and exposed to the nanorobots under motion (30 minutes UV-light exposure in 0.1% H_2O_2) and no-motion (30 min UV-light exposure) conditions. In contrast, PBS and H_2O_2 without nanorobots were used as control references. The bacteria viability was determined by testing four different concentrations of the nanorobots (200, 50, 5, and 0.5 μg mL^{-1}). The fluorescence (560/590 nm, excitation/emission) measured for the nanorobots indicated that 100 μg mL^{-1} was the MIC, and that 200 μg mL^{-1} were able to remove 92% of the biofilm under motion conditions, while only 18% of biofilm removal was achieved in the absence of motion. The results demonstrated how the enhanced solution mixing given by B-TiO_2/Ag nanorobots improves the reduction of the biofilm biomass helped by the combined effect of the enhanced ROS production and the quick penetration and diffusion of Ag ions through the biofilm and bacterial cell wall[27].

Encouraged by these preliminary data, the biofilm was grown onto titanium fixation plates. These devices are commonly used in the oral and maxillofacial surgery for bone fragments stabilization. Inhibition studies of the multispecies bacterial biofilm were led by monitoring the number of live and dead cells with fluorescence LIVE/DEAD assay. SYTO-9 and propidium iodide (PI) were used to label live (green) and dead (red) bacteria cells. Specifically, the titanium miniplates was incubated with 100 μg mL^{-1} of B-TiO_2/Ag nanorobots and exposed to UV-light for 30 minutes. As evidenced from **Figure 5**, the sample containing the nanorobots under motion conditions showed the highest efficacy counting 36% of dead bacteria. These results were also supported by SEM images of titanium miniplates after the treatment (**Figure S2**) and by determination of the brightness threshold calculated on digital microscope images, confirming how the motion induced in the B-TiO_2/Ag nanorobots can efficiently kill mature and resistant multispecies bacterial biofilm due to the synergistic effect between diffusion and enhanced release of ROS and Ag^+ ions.

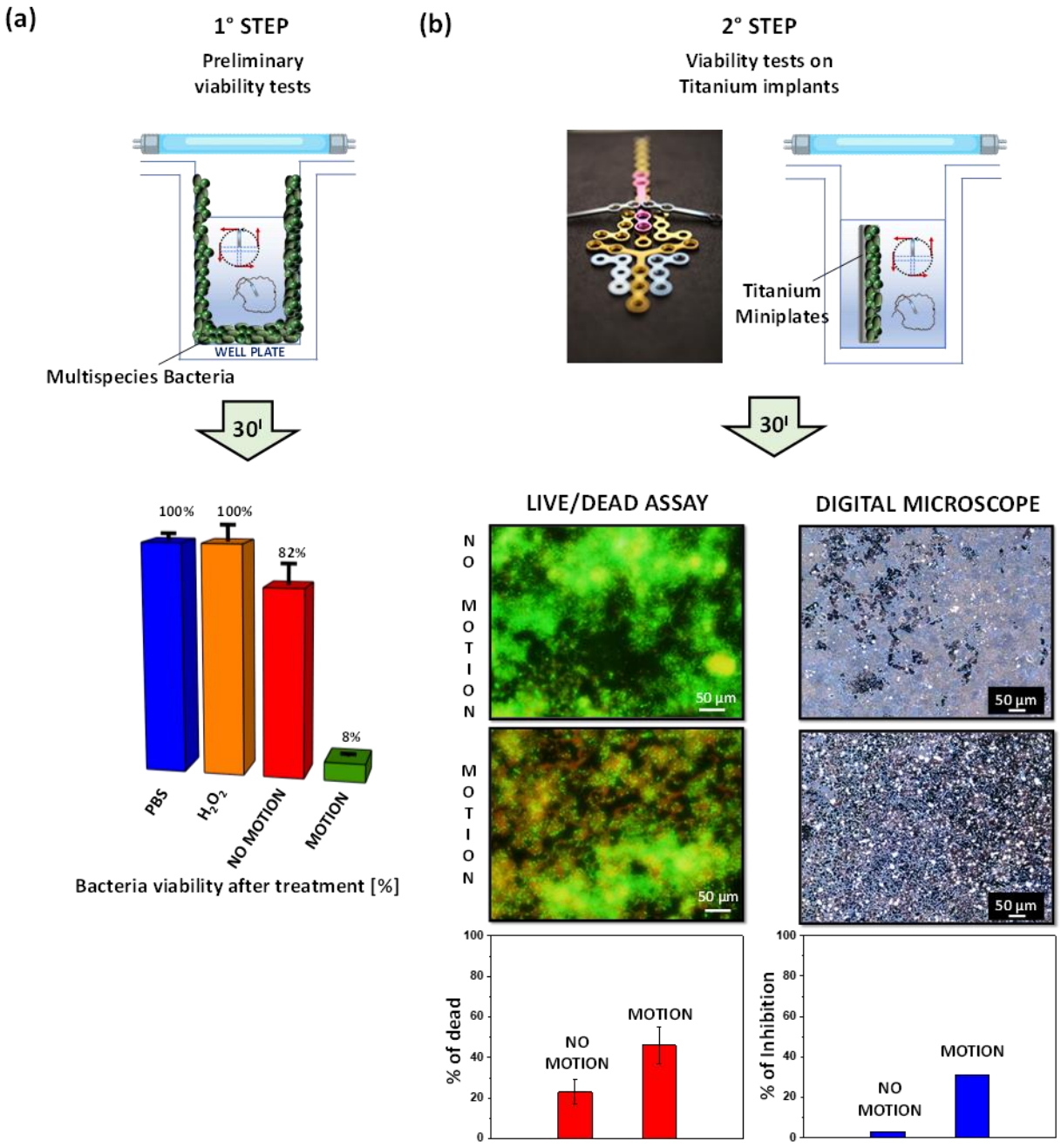

Figure 5. Antibiofilm experiments of light-propelled B-TiO_2/Ag nanorobots exposed to 30 minutes of UV-light irradiation in presence of 0.1% of H_2O_2. **(a)** Viability test of multispecies bacteria biofilm grown on polystyrene well plates treated with 100 µg mL^{-1} of B-TiO_2/Ag nanorobots under motion and static conditions. PBS and H_2O_2 in presence of self-propelled nanorobots were used as control references. **(b)** LIVE/DEAD 2D fluorescent images with corresponding percentage of dead bacteria cells (in red) and digital microscope images of residual multispecies biofilm onto titanium orthodontic implants with the corresponding inhibition percentage after treatment with static and moving B-TiO_2/Ag nanorobots.

Conclusion

In conclusion, we presented the first example of tubular nanorobots with extended light absorption wavelengths. Under both UV and blue-light irradiation, the black-TiO_2/Ag showed peculiar rotational and random propulsion modes with stop-go abilities by switching on-off the light. Specifically, under UV-light irradiation and in the presence of a very low amount of H_2O_2 (0.025%) the nanorobots showed self-propulsion activity. They registered a maximum speed of 500 ± 173 rpm min^{-1} and 31 ± 11 µm sec^{-1} in 0.1% H_2O_2 for rotational and random motion, respectively. Noticeably, the number of nanorobots undergoing the rotational motion decreased by increasing the wavelength of light irradiation. Also, the speed of the nanorobots moving randomly decreased to 11 ± 3 µm sec^{-1} under blue light illumination in 5% H_2O_2. This hindered motion is primarily due to faster surface recombination phenomena of the photogenerated electro-hole pairs.

The combined effect of autonomous movement and antibacterial activity of the B-TiO_2/Ag nanorobots allow their use as efficient nanotools for the removal of bacterial biofilm grown onto titanium orthodontic implants. According to the LIVE/DEAD assay results, the nanorobots were able to remove about 40% of the bacterial biofilm in 30 minutes under motion conditions. This results open a new route towards the study and treating most common dental implants (screws and plates), especially in removing bacterial communities among the microcavities between soft tissues and dental implants, which are difficult to reach and treat with conventional therapies.

Methods

Materials

Titanium foils were purchased from Sigma-Aldrich (thickness of 0.25 mm and 99.7% purity). Diethylene glycol (DEG, 99%), ammonium bi-fluoride salt (NH4F.HF) were purchased from Sigma-Aldrich (Merck, Germany). Ag target was purchased from Neyco (France). Methycillin-resistant *Staphylococcus aureus* (MRSA,CCM 7110) *Aggregatibacter actinomycetemcomitans* (CCM4688), and *Streptococcus mutans* (CCM7409) were obtained from the Czech Collection of Microorganisms (CCM, Brno, Czech Republic).

Preparation of separated TiO_2 nanotubes and reduction process (B-TiO_2 nanotubes)

Separated TiO_2 nanotubes were synthesized via electrochemical anodization of a titanium foil. The platinum sheet and the Ti foils were used as a counter and working electrodes respectively. The Ti foil with 2×1 cm in size, was first chemically cleaned by ultrasonication in acetone, ethanol, and deionized water for 15 min in each bath. Then, the foil was dried in nitrogen stream before being placed into the anodization setup. The electrochemical anodization was performed using a constant current voltage of 60 V at 35 °C for 2 h and the electrolyte contained 96 mL diethylene glycol, 0.6 wt.% NH_4F.HF, and 4 mL deionized (DI) water. Finally, all the synthesized samples were calcined at 450 °C in air for 2 h with heating and cooling rate of 2 °C/min. To prepare the reduced TiO_2 nanotubes, the samples were put in a tube furnace under H_2 atmosphere with flow rate 10 mL/min for 1 h at 450 °C.

Preparation of B-TiO_2/Ag nanorobots and motion analysis

30 nm of Ag layer was deposited on the B-TiO_2 nanotubes through a Leica EM ACE600 high vacuum sputter coater. Then, the obtained B-TiO_2/Ag nanorobots were removed from the Ti foil by a scalpel.

The nanorobots motion in the UV-light range was recorded in ultra-pure water in presence of different concentration of H_2O_2 (0.025, 0.1, and 0.5%) and exposed to 365 nm UV LED (Cool LED pE-100) operating at 1600 mW cm^{-2} light intensity. All videos were recorded at 50 fps and analyzed through Fiji Imaj software.

For visible light motion analysis two different filter cubes were used to

obtain two different light emissions: 450−470 nm (blue), and 540−550 nm (green). The two light emissions were used to study the self-propulsion abilities of the nanorobots and study the effect of wavelength on their propulsion actuation and speed. Furthermore, the effect of several concentrations of H_2O_2 (1, 2.3, and 5%) was monitored. All motion was recorded using a charge coupled device (CCD) camera at 20 frames per second with a magnification of 60X.

Antibiofilm experiments

Bacterial inoculum composed by MRSA, *Aggregatibacter actinomycetemcomitans* and *Streptococcus mutans* (1:1:1) was used for the multispecies biofilm growing.

For viability tests sterile biofilm was grown onto polystyrene cell wells. Every 24 hours fresh BHI medium was replaced. After 2-days the wells with biofilm were washed three times by PBS and treated by 4 different concentrations of B-TiO2/Ag nanorobots (200, 50, 5, and 0.5 μg/mL) with 0.1% of H2O2 and a sample without H_2O_2 was used as a reference sample. The treated samples were illuminated by a 365 nm UV lamp for 30 min. Afterwards, the plates were washed three times by PBS. To measure the bacteria cells viability all samples were treated with Alamar blue fluorescence stain in PBS (9:1) and the fluorescence (560/590 nm, excitation/emission) of the samples was measured.

LIVE/DEAD assay was measured on bacterial biofilm grown on Ti miniplates and treated with the nanorobots. Ti sheets were placed in 6-well cell culture plate, dipped in bacterial inoculum and incubated 5 hours. Afterwards, bacterial inoculum was replaced by fresh BHI+1% sucrose medium and incubated overnight. The biofilm was treated with samples (nanorobots and reference) dispersed in ultrapure water and 0.1% H_2O_2, at a concentration of 100 μg/ml (concentration chosen according to viability test) under UV-light irradiation for 30 minutes. As a control, 0.1% H_2O_2 was used. LIVE/DEAD bacteria cells were measured by BacLight Bacterial Viability and Counting Kit (Invitrogen) according to manufacturer's instructions.

Bacterial biofilm eradication on the surface of miniplates was also measured with a Keyence Digital Microscope VHX-5000 High-Resolution Zoom Lens VH-Z500R/Z500T (Mechelen, Belgium). Samples were prepared as mentioned above and biofilm surface coverage was determined based on the brightness threshold.

Numerical Simulation

The numerical simulation was carried out using the transport of diluted species module of the COMSOL Multiphysics software. For this purpose, the cross-section of the B-TiO_2/Ag nanorobots was considered. For the sake of simplicity, these were assumed as nanorods, rather than nanotubes, with a diameter of 200 nm and a length of 3 μm. The asymmetric and symmetric Ag coatings, corresponding to the rotating and swimming nanorobots, respectively, were designed by layers with a thickness of 30 nm, as shown in Figure 3(a). The H^+ generation due to the reaction between photogenerated holes in B-TiO_2 and H_2O_2 was simulated by choosing B-TiO_2/water boundaries as the generation ones. For this calculation, an H^+ diffusion coefficient in water at 25°C of 9.310×10^{-9} m^2 s^{-1} was used. Instead, the photogeneration rate was set to 1 mmol m^{-2} s^{-1}.

Characterization techniques

TESCAN MIRA3 XMU SEM equipped with an Oxford Instruments energy dispersive X-ray (EDX) detector was used to analyze the surface morphology and the elemental composition of B-TiO_2/Ag nanorobots.

To record all videos a Nikon ECLIPSE TS2R inverted microscope coupled to a BASLER acA1920-155uc digital camera was used. For digital microscopy, samples were observed directly in native state and images were evaluated by ImageJ graphic software.

Author contribution

M.Us. designed the experiments, prepared, characterized and tracked the nanorobots, interpreted the data and wrote the manuscript. S.K. synthesized the B-TiO_2 nanotubes. M.Ur. registered the nanorobots motion and carried out the numerical simulation. T.F., K.D. and V.A. performed the biological experiments. M.P and M.Us conceived the idea. M.P. supervised the research. All authors have given approval to the final version of the manuscript.

Acknowledgements

This work was supported by the ESF under the project CZ.02.2.69/0.0/0.0/18_053/0016962. CzechNanoLab project LM2018110 funded by MEYS CR is gratefully acknowledged for the financial support of the measurements/sample fabrication at CEITEC Nano Research Infrastructure. M.Ur. acknowledges the financial support by the European Union's Horizon 2020 research and innovation program under the Marie Skłodowska-Curie grant agreement No. 101038066.

References

(1) Al-Ahmad, A.; Wiedmann-Al-Ahmad, M.; Faust, J.; Bächle, M.; Follo, M.; Wolkewitz, M.; Hannig, C.; Hellwig, E.; Carvalho, C.; Kohal, R. Biofilm Formation and Composition on Different Implant Materials in Vivo. *J. Biomed. Mater. Res. - Part B Appl. Biomater.* **2010**, *95* (1), 101–109. https://doi.org/10.1002/jbm.b.31688.

(2) Choi, B. H.; Zhu, S. J.; Kim, Y. H. A Clinical Evaluation of Titanium Miniplates as Anchors for

Orthodontic Treatment. *Am. J. Orthod. Dentofac. Orthop.* **2005**, *128* (3), 382–384. https://doi.org/10.1016/j.ajodo.2005.04.016.

(3) Jhass, A. K.; Johnston, D. A.; Gulati, A.; Anand, R.; Stoodley, P.; Sharma, S. A Scanning Electron Microscope Characterisation of Biofilm on Failed Craniofacial Osteosynthesis Miniplates. *J. Cranio-Maxillofacial Surg.* **2014**, *42* (7), e372–e378. https://doi.org/10.1016/j.jcms.2014.03.021.

(4) Wang, D.; Haapasalo, M.; Gao, Y.; Ma, J.; Shen, Y. Antibiofilm Peptides against Biofilms on Titanium and Hydroxyapatite Surfaces. *Bioact. Mater.* **2018**, *3* (4), 418–425. https://doi.org/10.1016/j.bioactmat.2018.06.002.

(5) Minkiewicz-Zochniak, A.; Jarzynka, S.; Iwańska, A.; Strom, K.; Iwańczyk, B.; Bartel, M.; Mazur, M.; Pietruczuk-Padzik, A.; Konieczna, M.; Augustynowicz-Kopeć, E.; Olędzka, G. Biofilm Formation on Dental Implant Biomaterials by Staphylococcus Aureus Strains Isolated from Patients with Cystic Fibrosis. *Materials (Basel).* **2021**, *14* (8), 1–15. https://doi.org/10.3390/ma14082030.

(6) Lee, A.; Wang, H. L. Biofilm Related to Dental Implants. *Implant Dent.* **2010**, *19* (5), 387–393. https://doi.org/10.1097/ID.0b013e3181effa53.

(7) Do, T.; Devine, D.; Marsh, P. D. Oral Biofilms: Molecular Analysis, Challenges, and Future Prospects in Dental Diagnostics. *Clin. Cosmet. Investig. Dent.* **2013**, *5*, 11–19. https://doi.org/10.2147/CCIDE.S31005.

(8) Chen, Z.; Wang, Z.; Qiu, W.; Fang, F. Overview of Antibacterial Strategies of Dental Implant Materials for the Prevention of Peri-Implantitis. *Bioconjug. Chem.* **2021**, *32* (4), 627–638. https://doi.org/10.1021/acs.bioconjchem.1c00129.

(9) Silva, T. S. O.; Freitas, A. R.; Pinheiro, M. L. L.; Nascimento, C. Do; Watanabe, E.; Albuquerque, R. F. Oral Biofilm Formation on Different Materials for Dental Implants. *J. Vis. Exp.* **2018**, *2018* (136). https://doi.org/10.3791/57756.

(10) Huang, W.; Cheng, R.; Mao, L.; Zhao, Y. *Active Colloids: Toward an Intelligent Micromachine*; Elsevier Inc., 2018. https://doi.org/10.1016/B978-0-12-804069-0.00010-1.

(11) Urso, M.; Ussia, M.; Pumera, M. Breaking Polymer Chains with Self-Propelled Light-Controlled Navigable Hematite Microrobots. **2021**, *2101510* (91), 1–10. https://doi.org/10.1002/adfm.202101510.

(12) Wang, J.; Liu, X.; Qi, Y.; Liu, Z.; Cai, Y.; Dong, R. Ultrasound-Propelled Nanomotors for Improving

Antigens Cross-Presentation and Cellular Immunity. *Chem. Eng. J.* **2021**, *416* (February), 129091. https://doi.org/10.1016/j.cej.2021.129091.

(13) Dong, R.; Zhang, Q.; Gao, W.; Pei, A.; Ren, B. Highly Efficient Light-Driven TiO2-Au Janus Micromotors. *ACS Nano* **2016**, *10* (1), 839–844. https://doi.org/10.1021/acsnano.5b05940.

(14) Urso, M.; Iffelsberger, C.; Mayorga-Martinez, C. C.; Pumera, M. Nickel Sulfide Microrockets as Self-Propelled Energy Storage Devices to Power Electronic Circuits "On-Demand." *Small Methods* **2021**, *5* (10), 1–9. https://doi.org/10.1002/smtd.202100511.

(15) Soto, F.; Wang, J.; Ahmed, R.; Demirci, U. Medical Micro/Nanorobots in Precision Medicine. *Adv. Sci.* **2020**, *7* (21), 1–34. https://doi.org/10.1002/advs.202002203.

(16) Jurado-Sánchez, B.; Pacheco, M.; Rojo, J.; Escarpa, A. Magnetocatalytic Graphene Quantum Dots Janus Micromotors for Bacterial Endotoxin Detection. *Angew. Chemie - Int. Ed.* **2017**, *56* (24), 6957–6961. https://doi.org/10.1002/anie.201701396.

(17) Chandra, P.; Prakash, R. *Nanobiomaterial Engineering: Concepts and Their Applications in Biomedicine and Diagnostics*; 2020. https://doi.org/10.1007/978-981-32-9840-8.

(18) Ussia, M.; Urso, M.; Dolezelikova, K.; Michalkova, H.; Adam, V.; Pumera, M. Active Light-Powered Antibiofilm ZnO Micromotors with Chemically Programmable Properties. *Adv. Funct. Mater.* **2021**, *2101178*, 1–10. https://doi.org/10.1002/adfm.202101178.

(19) Peng, X.; Urso, M.; Pumera, M. Photo-Fenton Degradation of Nitroaromatic Explosives by Light-Powered Hematite Microrobots: When Higher Speed Is Not What We Go For. *Small Methods* **2021**, *5* (10), 1–9. https://doi.org/10.1002/smtd.202100617.

(20) Dai, B.; Wang, J.; Xiong, Z.; Zhan, X.; Dai, W.; Li, C. C.; Feng, S. P.; Tang, J. Programmable Artificial Phototactic Microswimmer. *Nat. Nanotechnol.* **2016**, *11* (12), 1087–1092. https://doi.org/10.1038/nnano.2016.187.

(21) Soto, F.; Karshalev, E.; Zhang, F.; Esteban Fernandez De Avila, B.; Nourhani, A.; Wang, J. Smart Materials for Microrobots. *Chem. Rev.* **2021**. https://doi.org/10.1021/acs.chemrev.0c00999.

(22) Jang, B.; Hong, A.; Kang, H. E.; Alcantara, C.; Charreyron, S.; Mushtaq, F.; Pellicer, E.; Büchel, R.; Sort, J.; Lee, S. S.; Nelson, B. J.; Pané, S. Multiwavelength Light-Responsive Au/B-TiO2 Janus Micromotors. *ACS Nano* **2017**, *11* (6), 6146–6154. https://doi.org/10.1021/acsnano.7b02177.

(23) Rajaraman, T. S.; Parikh, S. P.; Gandhi, V. G. Black TiO2: A Review of Its Properties and Conflicting Trends. *Chem. Eng. J.* **2020**, *389* (July 2019), 123918. https://doi.org/10.1016/j.cej.2019.123918.

(24) Chen, X.; Liu, L.; Huang, F. Black Titanium Dioxide (TiO2) Nanomaterials. *Chem. Soc. Rev.* **2015**, *44* (7), 1861–1885. https://doi.org/10.1039/c4cs00330f.

(25) Górska, P.; Zaleska, A.; Kowalska, E.; Klimczuk, T.; Sobczak, J. W.; Skwarek, E.; Janusz, W.; Hupka, J. TiO2 Photoactivity in Vis and UV Light: The Influence of Calcination Temperature and Surface Properties. *Appl. Catal. B Environ.* **2008**, *84* (3–4), 440–447. https://doi.org/10.1016/j.apcatb.2008.04.028.

(26) Foster, J. S.; Kolenbrander, P. E. Development of a Multispecies Oral Bacterial Community in a Saliva-Conditioned Flow Cell. *Appl. Environ. Microbiol.* **2004**, *70* (7), 4340–4348. https://doi.org/10.1128/AEM.70.7.4340-4348.2004.

(27) Ussia, M.; Urso, M.; Miritello, M.; Bruno, E.; Curcuruto, G.; Vitalini, D.; Condorelli, G. G.; Cantarella, M.; Privitera, V.; Carroccio, S. C. Hybrid Nickel-Free Graphene/Porphyrin Rings for Photodegradation of Emerging Pollutants in Water. *RSC Adv.* **2019**, *9* (52), 30182–30194. https://doi.org/10.1039/c9ra06328e.